ACS Sustainable Chemistry & Engineering

pubs.acs.org/journal/ascecg

Research Article

Enhanced Temperature Cycling of Particulate Reactors with Volumetric Induction Heating

Dorothy L. Mantle, Ariana B. Höfelmann, Zhennan Ru, Pinak Mohapatra, Chenghao Wan, Connor Cremers, Calvin H. Lin, Jian-Ping Shen, Andrew Tong, Juan Rivas-Davila, and Jonathan A. Fan*

Cite This: *ACS Sustainable Chem. Eng.* 2026, 14, 5922−5932

Read Online

ACCESS | Metrics & More | Article Recommendations | Supporting Information

ABSTRACT: The temperature cycling of reactor systems with solid particles is foundational to many processes in the chemicals industry. We present a clean energy platform for gas−solid temperature cycling based on induction heating, in which an open-cell metamaterial baffle loaded with solid particulates is internally heated in a volumetric, efficient, and fast manner. This platform offers flexible configurability, including operation as a fluidized or fixed-bed reactor at different stages of the temperature cycling process, where the baffle prevents bubble coalition during fluidized bed operation. We consider solid sorbents for carbon dioxide capture as a model system, and we demonstrate adsorption in a temperature-stabilized fluidized-bed mode and high-speed regeneration in a fixed-bed mode. Electrified temperature cycling with magnetic induction is scalable, and we anticipate its adaptation to a wide range of chemical conversion and separation processes.

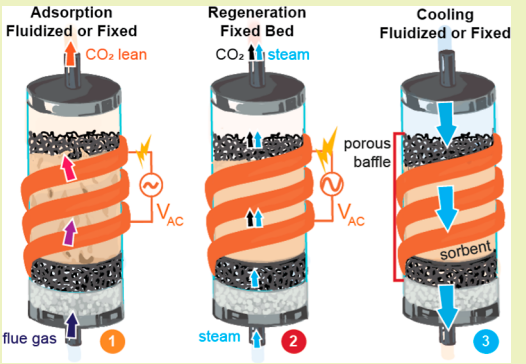

KEYWORDS: *fluidization, rapid TSA, metamaterial baffle, electrified heat*

1. INTRODUCTION

Temperature cycling of solid particles is utilized in many industrial processes, including chemical synthesis, energy storage, and gas separations.[1,2] In gas separations with solid sorbents,[3,4] which is the focus of this study, temperature swing adsorption (TSA) is an established technique in which gases are adsorbed into sorbents and then released in a regeneration step as a high-purity stream at elevated temperatures. A central theme in TSA implementation is the codesign of heat transfer, mass transfer, and pressure drop at different steps of the cycle, where adsorption and regeneration steps each require particular levels of temperature and mass transfer control with constraints set by an energy budget.[3,5−9] While TSA is industrially mature, it is still suboptimal due to nonidealities featured in conventional solids heating and heat integration schemes. Heating of fixed-bed systems with heating jackets (limited to below two meters in diameter) and heat exchange networks offer limited scaling as they are surface rather than volumetric heating methods and often generate large thermal gradients and hot spots.[10,11] Internal heating with hot gases, commonly steam, is energetically intensive and incompatible with many water-sensitive sorbents. The inefficient heat transfer and heating nonuniformity in all of these methods lead to relatively slow cycling times on the order of an hour or more.[12−14] In addition, conventional heat generation methods utilize carbon fuels and possess a nontrivial carbon footprint.

Concepts in electrified heating offer an alternative approach to heat integration in TSA that can enhance performance, cycling times, and energy efficiency as well as mitigate the carbon footprint of heating when using renewable electricity sources. Resistive heating of conductive composites with embedded sorbents and conductive monoliths packed with solid sorbents has been shown to enable uniform surface and volumetric heating within the bed.[15,16] Magnetic induction heating of sorbents embedded with susceptors has been found to facilitate the selective heating of susceptors and high heat transfer rates between the susceptor and sorbent.[17−23] Microwave heating has been demonstrated to support direct and selective sorbent heating with high power densities, leading to exceptionally fast regeneration times around 5 min or under, albeit with hot spots.[12,24] While these concepts show great promise, they still suffer from critical drawbacks, including electrical interconnect integration challenges in resistive heating networks, efficiency limitations in induction heating, and skin depth penetration, scaling, and hot spot limitations with microwave heating.[25,26] New concepts in electrified heating that maintain advantages in performance while overcoming these challenges are necessary.

Received: September 27, 2025
Revised: February 27, 2026
Accepted: March 2, 2026
Published: March 12, 2026

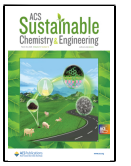

https://doi.org/10.1021/acssuschemeng.5c10443
ACS Sustainable Chem. Eng. 2026, 14, 5922−5932

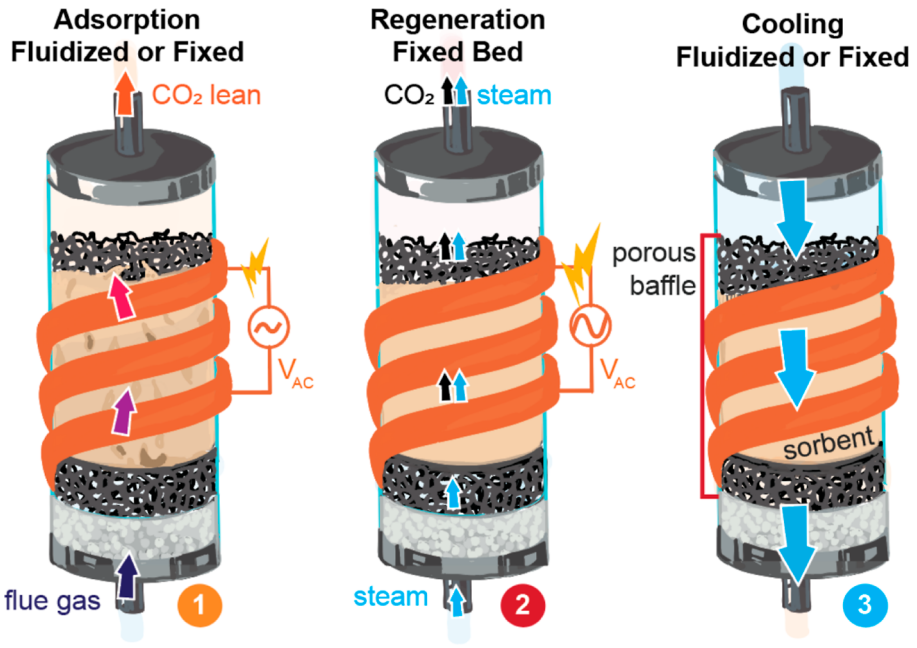

Figure 1. Temperature swing adsorption with solid sorbents and induction heating of a metamaterial baffle. Adsorption is performed in either fluidized or fixed-bed mode. In fluidized-bed mode, the baffle reduces bubble coalescence, improving mass transfer. Regeneration is performed in fixed-bed mode and is achieved by heating the baffle while flowing in steam as a sweeping gas. Cooling is performed by flowing gas into the system at a high flow rate in either the downward direction in fixed-bed mode or in the upward direction in fluidized-bed mode.

We propose a new concept in volumetric electrified heating for temperature-cycled reactors in which solid particles are placed in an open-cell, electrically conductive baffle that is inductively heated in an efficient, internal, volumetric, and fast manner. We term this baffle a "metamaterial susceptor" because it supports effective electromagnetic properties that are tunable based on geometry, and the bulk electrical conductivity can be designed to enable near-unity induction coupling efficiencies (i.e., selective heating of the susceptor over the coil). The baffle simultaneously serves as a volumetric heating source, a heat spreader that minimizes temperature gradients in the bed due to its high effective thermal conductivity, and a bubble breaker when the reactor is operated in fluidized-bed mode. We focus on carbon dioxide capture from flue gas streams as a model system and specifically consider potassium carbonate-based sorbents supported on porous alumina-silicate substrates. Potassium carbonate-based sorbents have an adsorption−desorption cycle based on a reversible chemisorption step

$$K_2CO_3(s) + CO_2(g) + H_2O(g) \leftrightarrow 2KHCO_3(s)$$
$$\Delta H_{rxn} = -143\ \text{kJ} \quad (1)$$

These alkali metal carbonate sorbents are attractive for point source capture applications because they are effective, cheap, do not degrade in humid environments, and can capture and release carbon dioxide at relatively low temperatures.[3,9] Among alkali metal carbonates, K_2CO_3 performs the best and has promising cost effectiveness at scale and absorbs optimally at 60 °C.[3,9] Porous supports for K_2CO_3 enable faster carbonation rates.[27] While many K_2CO_3 and support-based sorbents can be completely regenerated at 150 °C, some supports such as Al_2O_3 form products with K_2CO_3 that result in higher temperatures for complete regeneration.[28] Even in these more complex cases, the regeneration reaction, shown as the reverse reaction in eq 1, has a maximum rate at 150 °C.[13,28,29]

The operating principles of our reactor are summarized in Figure 1. During adsorption, the reactor can operate in either fixed or fluidized-bed mode, and induction heating of the baffle controls the volumetric bed temperature. Regeneration is performed with the sorbents in fixed-bed mode, during which the baffle is quickly and volumetrically heated by induction and the released carbon dioxide is swept away by a low-flow gas, commercial steam, which is later condensed, resulting in a pure stream of CO_2. The gas flow rate for regeneration is low, minimizing the energy cost of steam production, so fluidization, which requires a minimum gas velocity above that of the sweeping gas, should not be utilized. Cooling is performed by flowing a large stream of cool gas into the bed at high flow rates and can be done in either fixed or fluidized-bed mode. When cooling in fixed-bed mode, gases are top-fed, whereas gases are bottom-fed in fluidized-bed mode. Fluidization in either adsorption or cooling allows for lower pressure drops and greater heat transfer.

Our temperature cycling concept combines many of the advantageous features of electrified heating while managing many of the aforementioned challenges. First, it is a simple and versatile platform that can operate in different reactor bed configurations, and it does not require external heating infrastructure, electrode contacts, or modifications to sorbent particles such as the impregnation of heating susceptors. Second, regeneration can be performed quickly, as the susceptor can be rapidly and volumetrically heated with high power densities and supports large heat transfer rates to sorbents due to the susceptor's large surface area. Third, it is exceptionally efficient due to high heating rates and high coupling efficiency of electricity to internal heat due to the informed selection of power amplifier frequency, electrical conductivity, and thermal conductivity. Overall efficiency is further enhanced as the susceptor itself has a small thermal mass, and minimal amounts of sweeping gas during regeneration are required. Fourth, it can be readily scaled

https://doi.org/10.1021/acssuschemeng.5c10443
ACS Sustainable Chem. Eng. 2026, 14, 5922−5932

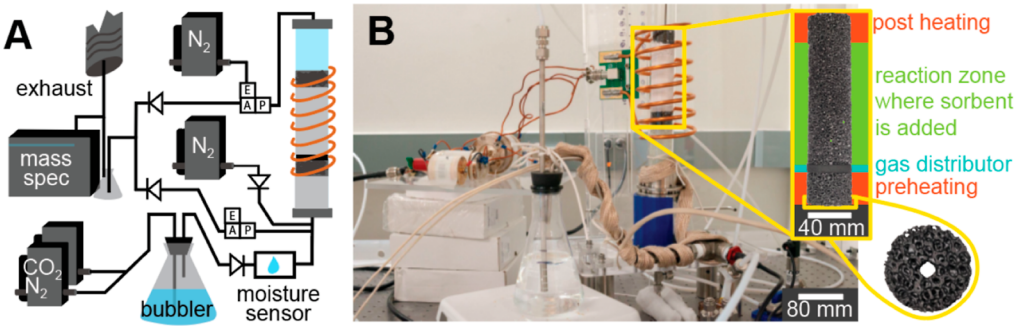

Figure 2. Experimental TSA demonstration. (A) Schematic of the experimental setup, which includes check valves, mass flow controllers, gas switches, a moisture sensor, and a mass spectrometer. (B) Image of the experimental setup. The inset shows an enlarged image of the reactor without the sorbent and shows the preheating, gas distributor, reaction, and post-heating zones.

due to the volumetric nature of induction heating and known scaling laws relating metamaterial susceptor electromagnetic properties, size, and induction frequency.[30]

2. MATERIALS AND METHODS

2.1. Sorbent Preparation

We prepared our sorbents as Geldart B-sized particles with an average diameter of 300 μm. Geldart B particles are selected due to their ease of synthesis and handling and their ability to fluidize at high velocities with limited bed expansion.[31] The sorbent is prepared by performing wetness impregnation of K_2CO_3 into porous aluminosilicate, where a 37% loading fraction is used. The aluminosilicate support is chosen due to its high surface area (450 m^2/g) and alkaline properties, which enable enhanced loading and erosion resistance.[32] More details on sorbent preparation and size distribution are included in Supporting Information.

2.2. TSA Reactor Setup

A schematic and image of our experimental TSA setup are shown in Figure 2A,B, respectively. The reactor consists of a quartz tube with an inner diameter of 39 mm that is sealed by two metallic flanges. The reactor is surrounded by a 25 mm thick thermal insulation layer of mineral wool (not shown for clarity) and a helical coil. The six-turn, 94 mm diameter coil is 150 mm in constructed length and consists of a copper tube with a diameter of 6 mm. The induction coil and flanges are mounted on acrylic holders that do not couple to the magnetic field generated by the induction coil. The reactor baffle and distributor are elevated within the tube by using glass beads to minimize coupling between the coil magnetic field and the flange at the bottom of the tube.

Inside the reactor, the 100 mm tall reaction zone consists of a reaction-bonded silicon carbide (i.e., SiSiC) foam metamaterial baffle loaded with sorbent particles. Silicon carbide-based monoliths are ideal from a heat management point of view because silicon carbide has a high thermal conductivity, enabling enhanced heat spreading within the reactor and the management of hot spots. The preheating and post-heating zones each comprise 25 mm-tall sections of the same SiSiC foam as in the reaction zone and do not contain sorbent powder. These zones mitigate axial temperature gradients in the reaction zone that naturally form at the top and bottom of the internally heated reactor due to heat loss at the ends. Between the preheating and reaction zones, a 3 mm-thick silicon carbide foam disk with an average pore size of 250 μm is placed and serves as the gas distributor. To measure the temperature within the reactor, a 4 mm-diameter hole is axially milled through the reaction zone and post-heating foam zone, enabling placement of a Hastelloy thermowell with a multipoint fiber optic temperature sensor. Fiber optic temperature sensors are used over thermocouples because they do not interact with high-frequency magnetic fields and provide fast temperature readings. Experimental temperature control used measurements from a fiber optic sensor located approximately 55 mm above the distributor.

Beyond axial temperature characterization of our system, we briefly remove insulation and use a midwave infrared camera (FLIR X6901sc) to characterize the surface temperature of the porous baffle and sorbent bed. Prior studies indicate that removal of the insulation leads to enhanced heat loss radially within the system but minimally impacts the axial temperature profile.[33] These infrared images are temperature-calibrated by tuning the emissivity of the reactor zone to match steady state temperature readings from a fiber optic within the sorbent reaction section held at 60 °C.

For the adsorption steps, the temperature of the reaction zone is maintained at 60 °C by inductively heating the baffle with fluctuating powers based on temperature feedback while flowing gas at the minimum fluidization velocity, u_{mf}. The duration of adsorption is dictated by the time required to reach 95% of the total sorbent adsorption capacity, which we measured to be 50 s using a mass spectrometer and show in Supporting Information. During regeneration, which occurs with reasonable kinetic rates between 120 and 170 °C, we send in a sweeping gas of nitrogen at 0.5 SLPM. Cooling at a given high gas flow can either be done using downflow, resulting in a fixed-bed mode with effective particle cooling without gas channeling or attrition at the expense of high pressure drop, or upflow, resulting in a fluidized-bed mode that supports cooling with reduced pressure drop conditions at the expense of particle attrition and the need for more infrastructure such as cyclones. For this study, we operate the reactor in a reverse flow fixed-bed mode and prioritize considerations in sorbent attrition and simplifications in reactor design. Thus, to perform cooling, nitrogen is flowed downward through the system at 8 SLPM.

To deliver power to our induction heating system, we set our function generator (Siglent SDG5162) to a sine wave at 6.78 MHz that is then passed to a power amplifier (E&I A1000 (300 kHz−35 MHz, 1 kW)). The power coming from the power amplifier is passed through an RF power meter (Agilent N1914A, N8428A) that reads the power going into and reflected from our matching network, coil, and inductively heated components. Our matching network is tuned such that our system appears to be a 50 Ω load to our power amplifier and power meter to maximize power delivery. The induction coil and susceptor together present mostly an inductive load, and a high-pass low-high matching network must be implemented to convert this impedance to a purely resistive load to ensure high power delivery to the susceptor. We construct the matching network using two variable vacuum capacitors (Jennings GCS-90-15S, 5−90 pF, and Comet CV1C-500NM/10, 80−500 pF).

Flue gas is simulated using a mixture of CO_2 and N_2 with a five percent CO_2 concentration, and moisture is added using a bubbler. More details on the setup are provided in the Supporting Information.

2.3. Hydrodynamics Characterization

To identify u_{mf} and further understand the impact of our metamaterial baffle on the hydrodynamic properties of our system, we perform differential pressure drop measurements through the sorbent bed at

https://doi.org/10.1021/acssuschemeng.5c10443
ACS Sustainable Chem. Eng. 2026, 14, 5922−5932

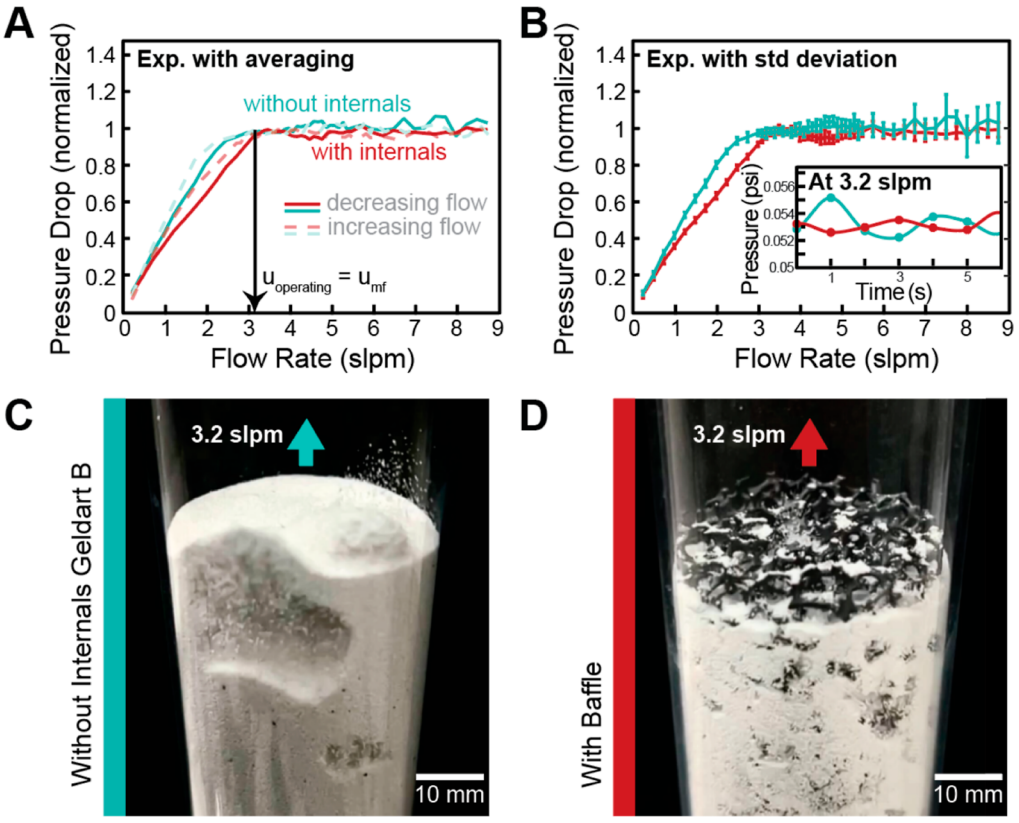

Figure 3. Hydrodynamics of solid sorbents in an open-cell baffle. (A) Hydrodynamic study of time-averaged pressure drop across sorbent powders, for the reactor system with and without the SiSiC foam baffle. Pressure drop is normalized relative to the weight of the sorbents. The minimum fluidization velocity when a baffle is present, which corresponds to our operating flow condition for adsorption, is demarcated as u_{mf} and is 3.2 SLPM. (B) Similar plot as in (A) but without time averaging. Inset: pressure drop as a function of time, given a flow rate of 3.2 SLPM. (C) Snapshot image of the reactor system without the SiSiC foam baffle, showing the formation of large bubbles even near u_{mf}. (D) Snapshot image of the reactor system with the SiSiC foam baffle, showing a reduction in bubble size.

different gas velocities with and without the metamaterial baffle. The tests are conducted by flowing nitrogen at room temperature into the reactor and utilizing a differential pressure gauge before the gas distributor and after the reactor outlet. To calculate the pressure drop across just the particles, pressure drop measurements of the bed with and without the metamaterial baffle are taken without and with sorbent particles sequentially. Subtraction of the reactor pressure drop without sorbent particles from the pressure drop with particles results in calibrated values of particle bed pressure drop for proper comparison.

2.4. Susceptor and Coil Electrical Characterization

We experimentally characterized our coil and SiSiC foam susceptor using small signal impedance measurements from a vector network analyzer (Bode 100) to quantify the AC resistance of the system. The AC resistance of the susceptor ($R_{susceptor}$) is obtained by subtracting the AC resistance measurement of just the coil (R_{coil}) from the AC resistance measurement of the coil with the susceptor. Coupling efficiency refers to the fraction of power dissipated in the susceptor relative to that of the coil and susceptor system, and it is calculated as $\eta_{coupling} = R_{susceptor}/(R_{susceptor} + R_{coil})$.

2.5. Multiphysics Heating Simulation Setup

To create a computational surrogate for our experimental reactor system, we utilize multiphysics finite element modeling using COMSOL Multiphysics. We utilize combined physics from electromagnetics using Maxwell's equations, free and porous media flow using time-independent Brinkman's equations, and heat transfer in solids and fluids using the transient solution of the heat equation. We simplify the gas flow by assuming an incompressible gas. We used a Darcy−Forchheimer model to account for the friction of the inserted baffle. To accurately fit the model with our experimental system, we perform a control experiment in which a constant power of 80 W is input into a regenerated sorbent-loaded reactor starting at 25 °C, the axial temperature is recorded as a function of time, and the reactor model is adjusted to fit these transient measurements. The thermal resistance between reactor components and the thermal conductivity of the fiber optic temperature sensor and thermowell are considered as fitting parameters, while realistic convection coefficients, porosities, thermal conductivities, densities, and heat capacities of the reactor components are kept fixed, as can be seen in the Supporting Information. Porous foams have been shown to facilitate homogenization of heating radially between phases, so we model our reaction zone to be a uniform porous medium with spherical pellets with an average diameter of 300 μm, which matches that of the average of the sorbent particles.[34]

3. RESULTS AND DISCUSSION

We implement a set of design principles to identify proper reactor configurations for electrified TSA systems. These design principles govern choices in susceptor construction and operational frequency that facilitate efficient and volumetric inductive heating, choices in the heating control approach that enable fast cycling with minimal energy input, and particle bed operating modes for enhanced mass transfer. We then utilize our designed parameters on a 39 mm-diameter lab scale setup, demonstrating cycles for point-source carbon capture.

3.1. Hydrodynamic Results

To perform adsorption, reactor configurations based on fixed beds, bubbling beds, and turbulent fluidized beds have been utilized in ways that are tailored and optimized for particular

https://doi.org/10.1021/acssuschemeng.5c10443
ACS Sustainable Chem. Eng. 2026, 14, 5922−5932

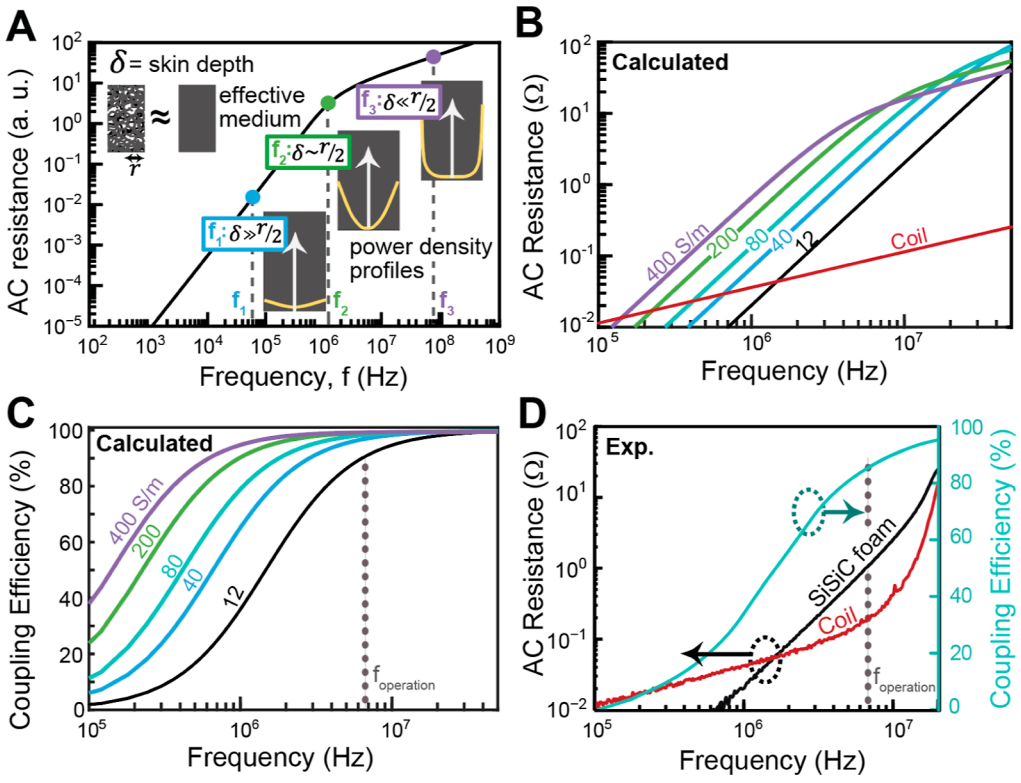

Figure 4. Electromagnetic properties of the metamaterial baffle. (A) The heating properties of the susceptor, modeled as an effective medium that is a homogeneous conductive cylinder, correlate with its AC resistance. Optimal conditions that correspond to regimes of volumetric and efficient heating are achieved when the susceptor skin depth is roughly half its radius (f_2). (B) Calculated AC resistance curves for homogeneous cylindrical susceptors with varying effective electrical conductivities together with the AC resistance curve of the magnetic coil. (C) Corresponding coupling efficiencies of the inductively heated systems from (B). (D) Experimental AC resistances of the susceptor and coil and corresponding coupling efficiency curve for the baffle and coil used in this study.

gas concentrations and sorbent types.[3,5−9] Fluidized beds, the focus here, have ideal heat transfer properties, eliminate hot spots, and process large volumes of gas per cycle. However, they suffer from poor mass transfer when gas bypasses the bed as bubbles.[35]

We aim to utilize the SiSiC foam baffle as a bubble breaker that balances wall effects, bubble-breaking capabilities, and a desire to easily load the sorbent and to operate the bed without a major pressure drop penalty. With these considerations in mind, we specify the SiSiC foam to have a pore density of ten pores per inch, which for our Geldart B particles corresponds to an average opening diameter of approximately eight times the effective sorbent particle diameter.

Characterization of the pressure drop in the sorbent-loaded system with and without the baffle is shown in Figure 3A,B. With and without the foam baffle, the pressure drop initially increases linearly with increasing superficial gas velocity until fluidization begins, as predicted by Ergun's equation for fixed-bed systems. At u_{mf}, the sorbents fluidize, and the pressure drop becomes constant as a function of flow rate. The normalized pressure drop after fluidization and the minimum fluidization velocities are comparable for the system with and without the baffle, indicating that the presence of our baffle does not contribute additional parasitic pressure drop in the system. We identify our system's u_{mf} to be 3.2 SLPM. We utilize this flow rate for the adsorption stage of CO_2 capture as it enables an ideal operation regime that features good heat and mass transfer properties, minimal particle attrition, and adequate residence times for high CO_2 recovery rates. Improved mass transfer at u_{mf} in our reactor is a result of the baffle disrupting bubble coalescence, keeping bubbles, that begin to form at u_{mf}, small.[36−39]

The ability of the SiSiC baffle to prevent bubble coalescence is evidenced by the relative reduction in pressure fluctuations when the SiSiC foam is used (Figure 3B). Pressure fluctuations are proportional to the size of the bubble and occur when a bubble breaks, often at the top of a fluidized bed. We observe that for a fluidized bed without a baffle, the pressure fluctuations steadily increase as flow increases, but when the baffle is present, the pressure fluctuations are nearly constant as a function of flow. With the baffle, fluctuations are reduced by 20% when the flow rate is at u_{mf} and by up to five times at flow rates around 8 SLPM. Evidence for reduction of bubble coalescence for enhanced mass transfer in fluidized beds can also be visually observed in images of the fluidized beds without and with the baffle, shown in Figure 3C,D, respectively. Without the baffle, large bubbles responsible for pressure fluctuations are clearly visible, whereas with the baffle, the bubbles all have size scales on the order of the foam pore size or smaller. We note that our foam bubble-breaking structure is distinctive from those often used in fluidized bed systems, which typically consist of single-layer discs or tubes of less structural complexity.[36−40] We reserve a more detailed analysis of hydrodynamics within highly structured baffle structures for a future study.

3.2. Metamaterial Baffle and Power Electronics Co-design

The second key design task involves proper specification of the induction heating-power electronics system in a manner that

https://doi.org/10.1021/acssuschemeng.5c10443
ACS Sustainable Chem. Eng. 2026, 14, 5922−5932

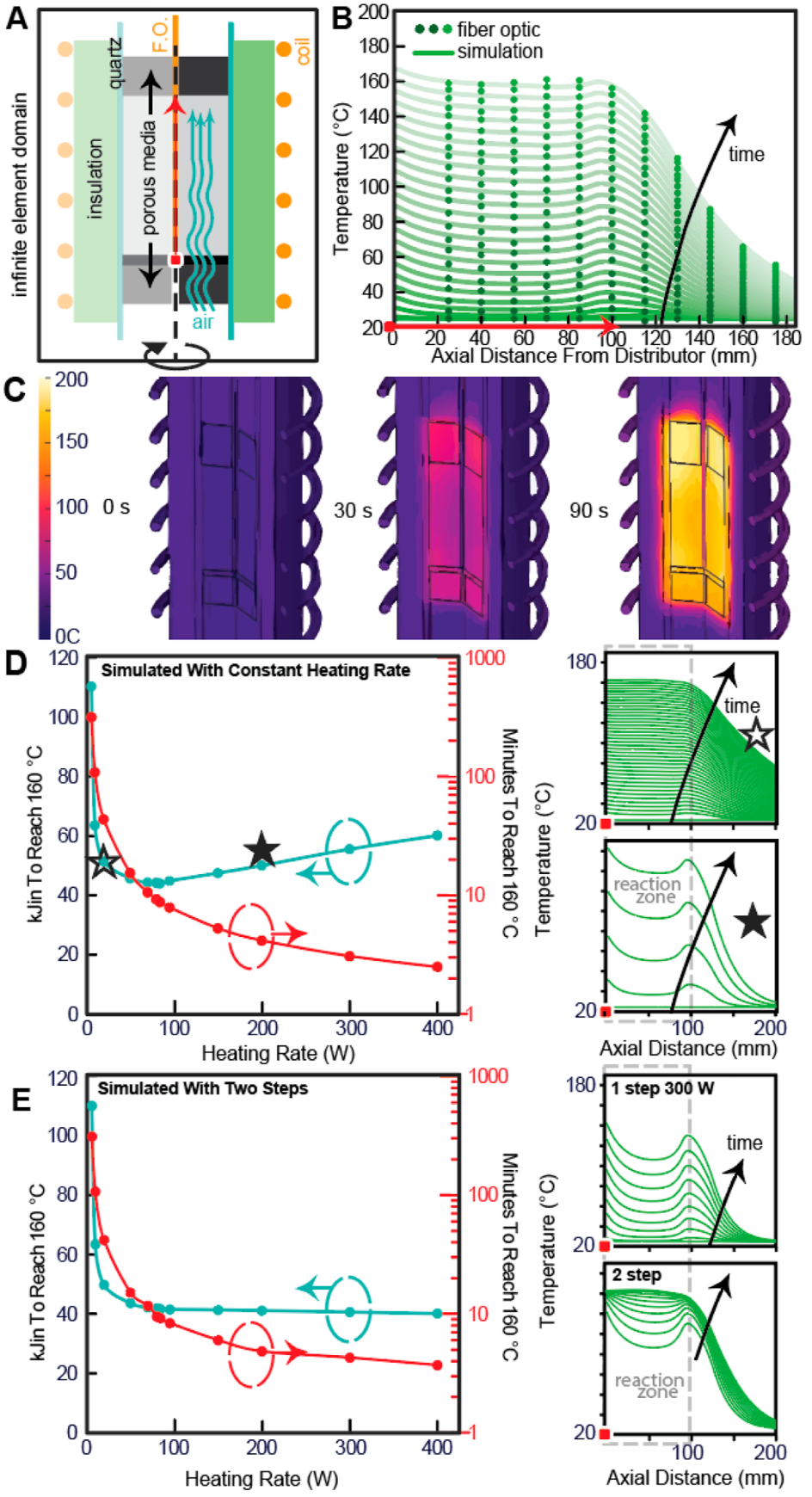

Figure 5. Dynamic heating analysis. (A) Multiphysics model setup. (B) Experimentally measured (dots) and simulated (lines) transient axial temperature profiles. (C) Simulated transient volumetric temperature profiles with a constant 400 W power input. (D) Plot of time and total energy input to heat the central axis of the reactor to 160 °C as a function of constant heating rates. Subplot curves each plotted 60 s apart. (E) Plot

https://doi.org/10.1021/acssuschemeng.5c10443
ACS Sustainable Chem. Eng. 2026, 14, 5922−5932

Figure 5. continued

of time and total energy input to heat the central axis of the reactor to 160 °C as a function of heating rate, given a two-step approach where a period of constant power input is followed by a time period where power is turned off. Subplot curves each plotted 15 s apart. The red curve plotted for minutes to reach 160 °C includes the time for both steps.

supports volumetric heating with a high coupling efficiency. To perform this analysis and optimization, we treat the macroscopic electromagnetic properties of the SiSiC foam as a homogeneous medium with an effective electrical conductivity (σ_{eff}), as seen in Figure 4A. In this picture, magnetic field penetration into the susceptor is characterized by the skin depth, $\delta = \sqrt{1/\pi\mu_0\sigma_{eff}f}$, where μ_0 is the permeability of free space and f is the frequency. When $\delta \sim r/2$, where r is the susceptor radius, the alternating current (AC) resistance curve of the susceptor has a transition point that corresponds to a heating regime with near maximal coupling efficiency and a desirable volumetric parabolic heating profile. Based on prior work, we have found that lab-scale SiSiC foams have such a transition point at megahertz frequencies and that, by operating at such high frequencies, induction heating can be performed with high coupling efficiencies.[33]

To further fine-tune our understanding of susceptor design for our lab-scale reactor form factor, we calculate the AC resistance of SiSiC foams ($R_{susceptor}$) with σ_{eff} ranging from 12 to 400 S/m (Figure 4B). This range reflects the ability for the electrical conductivity of SiSiC foams to be tuned based on excess silicon content and foam geometry.[41,42] The AC resistivity is derived as a function of frequency from Maxwell's equations, and solving the Helmholtz equation

$$R_{susc} = \frac{4\pi^2 f\mu_0 N^2 r^2}{L}\,\mathrm{Im}\left\{\frac{J_2\left((1+i)\frac{r}{\delta}\right)}{J_0\left((1+i)\frac{r}{\delta}\right)}\right\} \quad (2)$$

where L is the length of the coil and susceptor, J_n are Bessel functions of the nth order, and N is the number of turns of the coil. We also include a plot of the frequency-dependent AC resistance of the magnetic coil (R_{coil}) calculated using the improved Dowell method[43]

$$R_{coil} = \frac{\pi^{3/4} d N^{3/2}}{\sigma_c \delta_c \sqrt{R_c} L} \quad (3)$$

where R_c is the radius of the coil and d is the coil diameter. The coil resistance follows a square root of frequency trend, which is consistent with the regime in which the skin depth in the copper coil is less than the coil wall thickness. The foam resistances have transition point frequencies that scale inversely with conductivity, and the transition point frequency is approximately 5 MHz for the highest conductivity foam. The coupling efficiency is plotted in Figure 4C and shows that the efficiencies are generally high for all foams at megahertz frequencies. Marginal efficiency gains can be had in the limit where the foam conductivity is reduced, and the operating frequency is increased.

Based on these observations, we chose to operate our system at 6.78 MHz, which is the lowest standard industrial, scientific, and medical frequency band above 5 MHz, and aim to set our foam transition point to be near this frequency. While this condition does not maximize efficiency, coupling efficiencies are generally high at this frequency, and power amplifiers are known to have reduced efficiency, scalability, and susceptibility to parasitics as the operating frequency increases.[44] Due to availability, we utilize a SiSiC foam with a slightly suboptimal effective conductivity of 12 S/m. The AC resistances, together with experimentally derived coupling efficiency, are plotted in Figure 4D. The coil resistance scales as the square root of frequency, while the susceptor resistance scales as the square of frequency, both of which are consistent with our theoretical framework. The large rise in coil resistance at high frequencies is due to resonances in the coil system and does not impact coupling efficiency. The coupling efficiency curve also follows that from theoretical trends, and we measure this efficiency to be 86% at 6.78 MHz.

When the reactor is scaled up, the volumetric heating profile and high coupling efficiency can be maintained as long as $\delta \sim r/2$, similar to what is shown in Figure 4A. Skin depth can be adjusted in a number of different ways, including maintaining σ_{eff} while reducing f, maintaining f while reducing σ_{eff}, or by a combination of the two methods. In the limit where σ_{eff} is kept constant, the coupling efficiency remains the same, although more efficient and higher-power amplifiers can be implemented at lower frequencies. In the limit where f is kept constant, the coupling efficiency increases with the scale. A more detailed scaling analysis of inductively heated volumetric susceptors is presented elsewhere.[30]

3.3. Dynamic Heating Analysis

Our multiphysics model allows us to quantify the impact of the heating rate on the volumetric temperature profile within the reactor and optimize a control scheme for fast sorbent bed regeneration. Experimental and modeled axial temperature profiles for a power input of 80 W, measured every 18 s, are plotted in Figure 5B and show good agreement. With our fitted model, we can simulate heating at other power levels and visualize the volumetric temperature profile as a function of time. As an example, the volumetric temperature profiles for the reactor, given a steady input power of 400 W, are visualized at three different times in Figure 5C and show a reaction zone with a relatively uniform thermal profile at each time. These results also indicate that the axial temperature gradients measured by our fiber optic sensor near the post heating zone are mostly due to the thermowell serving as a heat sink and that the actual temperature profile within the reaction zone is much more uniform.

We use this model to perform parametric numerical heating experiments to understand and quantify the relationship between heating rate, energy efficiency (i.e., the total inputted energy required to heat the sorbent bed), and heating time. We are particularly interested in understanding how fast and efficiently we can heat, with an understanding that our use of a volumetric heating scheme overcomes some of the heat transfer bottlenecks associated with conventional heating methods. We considered two heating control schemes for regeneration. The first involves a direct one-step procedure in which the heating rate is fixed until the minimum temperature along the central axis of the reactor zone reaches 160 °C. The second is a two-step procedure in which the bed is first heated at a fixed rate to a temperature below 160 °C, and then the

https://doi.org/10.1021/acssuschemeng.5c10443
ACS Sustainable Chem. Eng. 2026, 14, 5922−5932

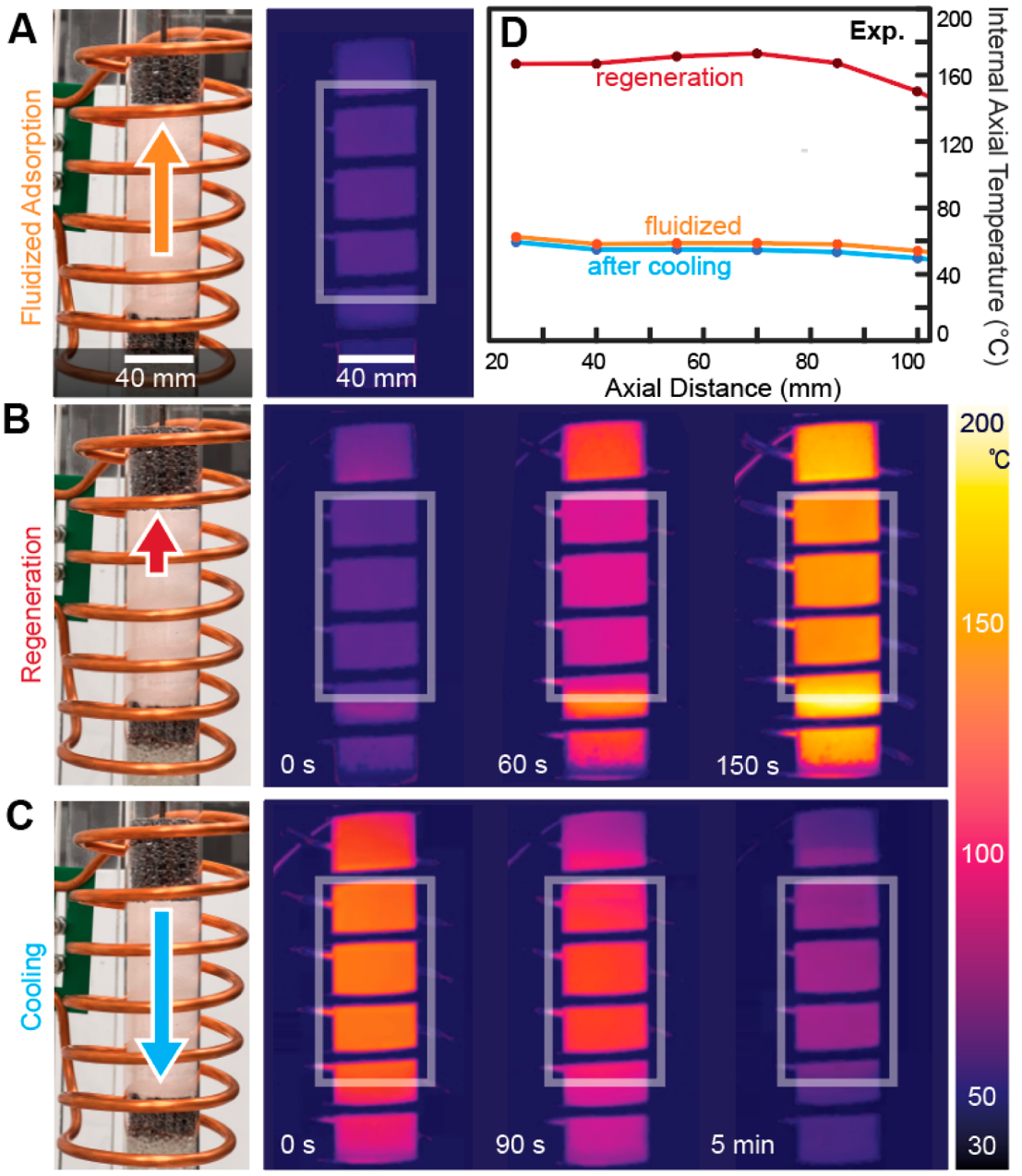

Figure 6. Thermal characterization of the TSA system. (A–C) Thermal images of the reactor taken during adsorption (A), regeneration (B), and cooling (C) steps. Photographs on the left of each figure show the sorbent bed height and relative gas flow. Bounding boxes indicate the reaction zone. (D) Axial temperature measurements within the sorbent bed taken from a multipoint fiber optic temperature sensor at the end of adsorption, regeneration, and cooling steps. Axial distance is measured starting from the top of the gas distributor.

power is shut off, during which time axial temperature gradients are leveled such that the reaction zone reaches 160 °C. The first step heating time is optimized by simulations to ensure the entire axial reaction zone temperature rises to 160 °C in the second step before dropping to ambient temperatures.

Starting from 25 °C, the transient axial temperature profile, energy consumption values, and temperature ramping time for the one-step heating process are summarized in Figure 5D. We find that as the heating rate increases, a monotonic decrease in heating time is observed, indicating that extreme regeneration times are possible. The total amount of energy consumption initially decreases as a function of heating rate to a minimum value near a heating rate of 84 W, after which it slowly increases. The initial reduction in power consumption is due to the fact that as the heating rate increases, there is less time for energy to be transported away from the reaction zone to the ambient at the ends of the reactor and through the thermal insulation. In this regime, the transient axial thermal profiles are relatively isothermal within the reaction zone and uniformly increase with time. At higher heating rates beyond the inflection point in power consumption, axial temperature gradients start to appear within the reaction zone with a peak near the outer edges of the zone. These arise because the heat capacity of the pre- and postheating zones is lower than that of the reaction zone, and the heating rate exceeds the rate of heat transfer from the axial edges to the center of the reaction zone.

https://doi.org/10.1021/acssuschemeng.5c10443
ACS Sustainable Chem. Eng. 2026, 14, 5922–5932

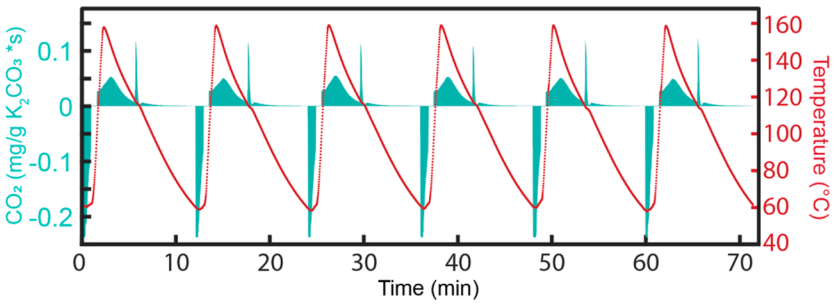

Figure 7. Experimental TSA results showing temperature ramping and cooling with capture and release of CO_2 over six cycles. The shaded regions indicate the amount of normalized CO_2 captured or released per adsorption or regeneration step.

With this accentuated thermal time delay, the axial edges of the reaction zone get overheated, leading to excess energy usage.

This overheating problem is addressed with our two-step method, shown in Figure 5E, also with an initial temperature of 25 °C. This simple control protocol ensures that some excess heat generated at the reaction zone edges transfers to the zone center. Due to the enhanced effective thermal conductivity of all reactor zones supported by the SiSiC baffle and the low thermal conductivity of our insulation, the temperature gradient within the reaction zone decreases during the second step. We find with our two-step method that increases in the heating rate lead to a plateauing of energy consumption while still reducing heating time. With this in mind, we select to use a two-step approach with an initially high heating rate for efficient energy use and fast cycling.

The regeneration of K_2CO_3 on an aluminate-based support has been previously shown to have a dependence on heating rates, and full regeneration occurs in three different stages, each with different temperatures.[28,45] The predominant stage is the reverse reaction of eq 1 and accounts for 76% of the CO_2 release, which has a maximum kinetic rate that occurs at 150 °C.[45] As it is the goal of this study to demonstrate fast heating rates and short cycle times for the reaction in eq 1, we do not cycle to the higher temperatures required for the two other stages of regeneration and use only a portion of our sorbent in each cycle. Given our limited sorbent utilization, the actual energy consumed by the reaction during cycling is small compared to that required to heat the reaction zone. As such, our surrogate model does not account for the particular reaction heat consumption of the regeneration process.

Considering the trade-off in kinetics and heating rates, which is specific to our sorbent, the ideal heating rate for both energy efficiency and kinetics is 35 °C per minute,[28] which would require a heating rate of around 200 W using the two-step heating approach. However, as the goal of the demonstration is to showcase fast heating rates, we chose a higher heating rate of 350 W for the cycling demonstration. This dynamic heating analysis would need to be considered in tandem with specific reaction kinetics for other temperature cycling processes. When using the two-step heating approach for regeneration with a 350 W for the first stage, we found that upon shutting the power off for the second stage, the bed temperature continued to rise until our temperature control point reached 160 °C. This two-step approach ensured that the entire reaction zone reached at least 150 °C. The total time required for heating from 60 to 160 °C and the sorbents to be regenerated is measured to be around four and a half minutes. The time required for cooling is then measured to be around six and a half minutes.

3.4. Temperature Uniformity during TSA

Temperature characterization of our system using complementary analyses of infrared imaging and multipoint fiber optic temperature sensing indicates that the temperature of the reaction zone is relatively uniform at all points of the TSA process. Experimental axial measurements (Figure 6D) show that within the reaction zone, a minimal temperature gradient of <8 °C exists for fluidized adsorption, which is expected given the heat transfer benefits of fluidized beds. The measured temperature profile within the reaction zone during regeneration is mostly uniform except near the region at the reaction zone-post heating zone interface, which is mostly an artifact from the thermowell acting as a cold sink, as described earlier with our multiphysics finite element modeling. Due to differences in emissivities in the different sections of the reactor, only the temperatures within the bounding box of the sorbent reactor section are considered.

3.5. Cycling Results

We performed six continuous cycles of CO_2 adsorption, regeneration, and cooling in our system, as shown in Figure 7. Positive values represent regenerated milligrams of CO_2 per gram of K_2CO_3, while negative values represent adsorbed amounts. The positive sharp peak in each cycle occurs during the onset of cooling when the flow rate changes quickly from a low sweeping gas flow rate to a large cooling gas flow rate. This peak was used to synchronize the time between the gas analyzer readings (which are delayed due to the length of the gas outlet line) and near-instantaneous measurements such as temperature and mass flow rates. On average, 8.8 mg of CO_2/g K_2CO_3 is both captured and released each cycle with a standard deviation of 0.16 mg of CO_2/g K_2CO_3. The average difference in how much was regenerated and adsorbed per cycle, represented by the difference in the shaded regions, is on average 0.016 mg of CO_2/g K_2CO_3 with a standard deviation of 0.30 mg of CO_2/g K_2CO_3 which is likely a result of the uncertainty of exact time of transitioning between regeneration and adsorption gas readings due to gas mixing and not utilizing the sorbent to its full capacity, as described in the experimental heating rate section. Each cycle takes about 12 min, including cooling time.

4. CONCLUSIONS

This study represents the first of its kind to combine the inductive heating of a porous baffle with a fluidized-bed system. Our concepts enable enhanced levels of performance for TSA processes, as they capitalize on the ability of structured baffles to serve as enhanced bubble breakers and volumetric heating elements with high effective thermal

https://doi.org/10.1021/acssuschemeng.5c10443
ACS Sustainable Chem. Eng. 2026, 14, 5922−5932

conductivities. By performing adsorption, regeneration, and cooling steps all in the same reactor, our concept supports considerable simplifications in the reactor design. We anticipate that our concept can adapt to other TSA processes and that it is particularly suited for temperature cycle reaction processes in which fluidization benefits the exothermic stage with reduction of hot spots and temperature stabilization, while inductive heating facilitates fast heating rates and energy savings when ramping to endothermic reaction temperatures. In our particular demonstration, we reached regeneration temperatures under 2 min with volumetric heating and low thermal gradients. We also anticipate that our concept can be readily adapted to circulating fluidized-bed systems, many of which utilize heating for solid particle regeneration.

In this study, we chose to operate near the minimum fluidization velocity during adsorption to balance the residence time, temperature homogenization, and particle attrition considerations. We anticipate that for reactions with sufficiently good capture kinetics and more mechanically robust sorbent particles, operation at higher gas flow rates is possible and enabled by the excellent bubble-breaking characteristics of the baffle. As we consider scaled system implementation, we anticipate new system-level architectures for the TSA reactor design. To accommodate steady-state point-source gas flows, an ensemble of inductively heated reactors can be utilized in which a fraction of reactors at any given time is being regenerated, while the rest of the reactors are operated in adsorption mode. An ensemble of reactors can also facilitate more effective modes of heat integration in which the sorbent cooling process is used effectively for gas preheating. We plan to systematically examine different systems-level TSA architectures in future work to understand and quantify the heat utilization efficiency limits of this class of systems.

■ ASSOCIATED CONTENT

Supporting Information

The Supporting Information is available free of charge at https://pubs.acs.org/doi/10.1021/acssuschemeng.5c10443.

Additional information on sorbent size, breakthrough curves, sorbent capacity, setup, and modeling properties (PDF)

■ AUTHOR INFORMATION

Corresponding Author

Jonathan A. Fan − *Department of Electrical Engineering, Stanford University, Stanford, California 94305-4088, United States;* orcid.org/0000-0001-9816-9979; Email: jonfan@stanford.edu

Authors

Dorothy L. Mantle − *Department of Mechanical Engineering, Stanford University, Stanford, California 94305-4088, United States;* orcid.org/0009-0007-8147-3684

Ariana B. Höfelmann − *Department of Electrical Engineering, Stanford University, Stanford, California 94305-4088, United States*

Zhennan Ru − *Department of Material Science Engineering, Stanford University, Stanford, California 94305-4088, United States*

Pinak Mohapatra − *Department of Electrical Engineering, Stanford University, Stanford, California 94305-4088, United States*

Chenghao Wan − *Department of Electrical Engineering, Stanford University, Stanford, California 94305-4088, United States;* orcid.org/0000-0002-4132-4779

Connor Cremers − *Department of Electrical Engineering, Stanford University, Stanford, California 94305-4088, United States*

Calvin H. Lin − *Department of Electrical Engineering, Stanford University, Stanford, California 94305-4088, United States*

Jian-Ping Shen − *Susteon Inc., Morrisville, North Carolina 27560, United States*

Andrew Tong − *Susteon Inc., Morrisville, North Carolina 27560, United States*

Juan Rivas-Davila − *Department of Electrical Engineering, Stanford University, Stanford, California 94305-4088, United States*

Complete contact information is available at: https://pubs.acs.org/10.1021/acssuschemeng.5c10443

Notes

The authors declare no competing financial interest.

■ ACKNOWLEDGMENTS

J.A.F. and J.R.-D. acknowledge support from the Department of Energy under agreement number DE-EE0011191 and from Stanford's Strategic Energy Research Consortium under agreement number AW1077664. D.L.M. acknowledges support from the TomKat Center for Sustainable Energy Graduate Fellowship and National Science Foundation Graduate Research Fellowship. A.B.H., C.C., and C.H.L. acknowledge support from the Stanford Graduate Fellowship.

■ REFERENCES

(1) Oudejans, D.; Offidani, M.; Constantinou, A.; Albonetti, S.; Dimitratos, N.; Bansode, A. A Comprehensive Review on Two-Step Thermochemical Water Splitting for Hydrogen Production in a Redox Cycle. *Energies* **2022**, *15*, 3044.

(2) Alsahlani, A.; Ozalp, N.; Randhir, K.; Hayes, M.; Schimmels, P.; Klausner, J. A reduced-order modeling of a tubular solar reactor for long duration thermochemical energy storage. *J. Energy Storage* **2023**, *67*, 107465.

(3) Boonprasop, S.; Chalermsinsuwan, B.; Piumsomboon, P. Effect of the operating parameters on the CO2 capture capacity of potassium carbonate supported on gamma alumina (K2CO3/γ-Al2O3) using conventional heat regeneration. *J. Taiwan Inst. Chem. Eng.* **2017**, *78*, 282−289.

(4) Prajapati, A.; Renganathan, T.; Krishnaiah, K. Kinetic Studies of CO2 Capture Using K2CO3/Activated Carbon in Fluidized Bed Reactor. *Energy Fuels* **2016**, *30*, 10758−10769.

(5) Jongartklang, N.; Chanchairoek, S.; Piumsomboon, P.; Chalermsinsuwan, B. Correlations of kinetic parameters with various system operating conditions for CO2 sorption using K2CO3/Al2O3 solid sorbent in a fixed/fluidized bed reactor. *J. Environ. Chem. Eng.* **2016**, *4*, 1938−1947.

(6) Jasi, A. Air Apparents. https://www.thechemicalengineer.com/features/air-apparents/ (accessed March 20, 2025).

(7) Spenik, J.; Resnik, K.; Hoffman, J.; Hopkinson, D. *Carbon Capture Unit (C2U) Design and Experimental Results Using Polyethylenimene (PEI) Immobilized on Mesoporous Silicas*, Technical Report; National Carbon Capture Center, 2014.

(8) Wang, D.; Joshi, A.; Fan, L.-S. Chemical looping technology − a manifestation of a novel fluidization and fluid-particle system for CO2

capture and clean energy conversions. *Powder Technol.* **2022**, *409*, 117814.
(9) Jaiboon, O.-a.; Chalermsinsuwan, B.; Mekasut, L.; Piumsomboon, P. Effect of flow patterns/regimes on CO2 capture using K2CO3 solid sorbent in fluidized bed/circulating fluidized bed. *Chem. Eng. J.* **2013**, *219*, 262−272.
(10) Ntiamoah, A.; Ling, J.; Xiao, P.; Webley, P. A.; Zhai, Y. CO2 Capture by Temperature Swing Adsorption: Use of Hot CO2-Rich Gas for Regeneration. *Ind. Eng. Chem. Res.* **2016**, *55*, 703−713.
(11) Yang, W.-C.; Hoffman, J. Exploratory Design Study on Reactor Configurations for Carbon Dioxide Capture from Conventional Power Plants Employing Regenerable Solid Sorbents. *Ind. Eng. Chem. Res.* **2009**, *48*, 341−351.
(12) Jang, G. G.; Kasturi, A.; Stamberga, D.; Custelcean, R.; Keum, J. K.; Yiacoumi, S.; Tsouris, C. Ultra-fast microwave regeneration of CO2 solid sorbents for energy-efficient direct air capture. *Sep. Purif. Technol.* **2023**, *309*, 123053.
(13) Hartman, M.; Svoboda, K.; Čech, B.; Pohořelý, M.; Šyc, M. Decomposition of Potassium Hydrogen Carbonate: Thermochemistry, Kinetics, and Textural Changes in Solids. *Ind. Eng. Chem. Res.* **2019**, *58*, 2868−2881.
(14) Bonjour, J.; Clausse, M.; Meunier, F. A TSA process with indirect heating and cooling: parametric analysis and scaling-up to practical sizes. *Chem. Eng. Process.* **2005**, *44*, 969−977.
(15) Thompson, J. F.; Bellerjeau, C.; Marinick, G.; Osio-Norgaard, J.; Evans, A.; Carry, P.; Street, R. A.; Petit, C.; Whiting, G. L. Intrinsic Thermal Desorption in a 3D Printed Multifunctional Composite CO2 Sorbent with Embedded Heating Capability. *ACS Appl. Mater. Interfaces* **2019**, *11*, 43337−43343.
(16) Zanco, S. E.; Ambrosetti, M.; Groppi, G.; Tronconi, E.; Mazzotti, M. Heat transfer intensification with packed open-cell foams in TSA processes for CO2 capture. *Chem. Eng. J.* **2022**, *430*, 131000.
(17) Woodliffe, J. L.; Johnston, A.-L.; Fay, M.; Ferrari, R.; Gomes, R. L.; Lester, E.; Ahmed, I.; Laybourn, A. Rapid microwave synthesis of sustainable magnetic framework composites of UTSA-16(Zn) with Fe_3O_4 nanoparticles for efficient CO2 capture. *Mater. Adv.* **2023**, *4*, 5838−5849.
(18) Newport, K.; Baamran, K.; Rownaghi, A. A.; Rezaei, F. Magnetic-Field Assisted Gas Desorption from Fe2O3/Zeolite 13X Sorbent Monoliths for Biogas Upgrading. *Ind. Eng. Chem. Res.* **2022**, *61*, 18843−18853.
(19) Schoukens, M.; Gholami, M.; Baron, G. V.; Van Assche, T.; Denayer, J. F. M. Hybrid induction vacuum swing adsorption, a rapid and fully electrified carbon capture process. *Chem. Eng. J.* **2023**, *459*, 141587.
(20) Bellusci, M.; Masi, A.; Albino, M.; Peddis, D.; Petrecca, M.; Sangregorio, C.; La Barbera, A.; Varsano, F. Fe3O4@HKUST-1 magnetic composites by mechanochemical route for induction triggered release of carbon dioxide. *Microporous Mesoporous Mater.* **2021**, *328*, 111458.
(21) Gholami, M.; Verougstraete, B.; Vanoudenhoven, R.; Baron, G. V.; Van Assche, T.; Denayer, J. F. M. Induction heating as an alternative electrified heating method for carbon capture process. *Chem. Eng. J.* **2022**, *431*, 133380.
(22) Idakiev, V. V.; Marx, S.; Roßau, A.; Bück, A.; Tsotsas, E.; Mörl, L. Inductive heating of fluidized beds: Influence on fluidization behavior. *Powder Technol.* **2015**, *286*, 90−97.
(23) Sunny, A.; Kudva, I. K.; Shinde, S.; Aranha, D.; Pandit, K.; Gun, S.; Mohapatra, P.; Wang, D.; Tong, A.; Fan, L.-S. Enhancing Carbon Capture Efficiencies in Natural Gas Power Plants through Magnetic Stabilization of Fluidized Beds, *2024 AIChE Annual Meeting*, 2024.
(24) Gomez-Rueda, Y.; Verougstraete, B.; Ranga, C.; Perez-Botella, E.; Reniers, F.; Denayer, J. F. M. Rapid temperature swing adsorption using microwave regeneration for carbon capture. *Chem. Eng. J.* **2022**, *446*, 137345.
(25) Grande, C. A.; Ribeiro, R. P. L.; Oliveira, E. L. G.; Rodrigues, A. E. Electric swing adsorption as emerging CO2 capture technique. *Energy Procedia* **2009**, *1*, 1219−1225.
(26) An, H.; Feng, B.; Su, S. CO2 capture by electrothermal swing adsorption with activated carbon fibre materials. *Int. J. Greenhouse Gas Control* **2011**, *5*, 16−25.
(27) Zhao, C.; Chen, X.; Zhao, C. K2CO3/Al2O3 for Capturing CO2 in Flue Gas from Power Plants. Part 1: Carbonation Behaviors of K2CO3/Al2O3. *Energy Fuels* **2012**, *26*, 1401−1405.
(28) Zhao, C.; Chen, X.; Zhao, C. K2CO3/Al2O3 for Capturing CO2 in Flue Gas from Power Plants. Part 2: Regeneration Behaviors of K2CO3/Al2O3. *Energy Fuels* **2012**, *26*, 1406−1411.
(29) Zhao, W.; Sprachmann, G.; Li, Z.; Cai, N.; Zhang, X. Effect of K2CO3· 1.5H2O on the regeneration energy consumption of potassium-based sorbents for CO2 capture. *Appl. Energy* **2013**, *112*, 381−387.
(30) Wan, C.; Cremers, C.; Höfelmann, A. B.; Ru, Z.; Lin, C. H.; Tamakuwala, K. N.; Mantle, D.; Mohapatra, P.; Rivas-Davila, J.; Kanan, M. W.; Fan, J. A. Scale Up Analysis of Inductively Heated Metamaterial Reactors. *arXiv* **2025**, arXiv:2509.13719.
(31) Geldart, D. Expansion of Gas Fluidized Beds. *Ind. Eng. Chem. Res.* **2004**, *43*, 5802−5809.
(32) Zhao, C.; Chen, X.; Zhao, C. K2CO3/Al2O3 for Capturing CO2 in Flue Gas from Power Plants. Part 4: Abrasion Characteristics of the K2CO3/Al2O3 Sorbent. *Energy Fuels* **2012**, *26*, 1395−1400.
(33) Lin, C. H.; Wan, C.; Ru, Z.; Cremers, C.; Mohapatra, P.; Mantle, D. L.; Tamakuwala, K.; Höfelmann, A. B.; Kanan, M. W.; Rivas-Davila, J.; Fan, J. A. Electrified thermochemical reaction systems with high-frequency metamaterial reactors. *Joule* **2024**, *8*, 2938−2949.
(34) Razza, S.; Heidig, T.; Bianchi, E.; Groppi, G.; Schwieger, W.; Tronconi, E.; Freund, H. Heat transfer performance of structured catalytic reactors packed with metal foam supports: Influence of wall coupling. *Catal. Today* **2016**, *273*, 187−195.
(35) Miracca, I.; Capone, G. The staging in fluidised bed reactors: from CSTR to plug-flow. *Chem. Eng. J.* **2001**, *82*, 259−266.
(36) Rennebaum, H. S.; Brummerloh, D. L.; Benders, S.; Penn, A. The effect of baffles on the hydrodynamics of a gas-solid fluidized bed studied using real-time magnetic resonance imaging. *Powder Technol.* **2024**, *432*, 119114.
(37) Feng, X.; Shen, L.; Wang, L. Effect of baffle on hydrodynamics in the air reactor of dual circulating fluidized bed for chemical looping process. *Powder Technol.* **2018**, *340*, 88−98.
(38) Zhang, Y. *Essentials of Fluidization Technology*; Wiley, 2020; pp 431−455.
(39) Kunii, D.; Levenspiel, O. Fluidization Engineering. *Butterworth-Heinemann Series in Chemical Engineering*, 2nd ed.; Butterworth-Heinemann, 1991; pp 20−220.
(40) Ahmed, I.; DucSesne, M.; Tan, Y.; Lu, D. Y. Electrically Heated Fluidized Beds A Review. *Ind. Eng. Chem. Res.* **2024**, *63*, 4205−4235.
(41) Ortona, A.; D'Angelo, C.; Gianella, S.; Gaia, D. Cellular ceramics produced by rapid prototyping and replication. *Mater. Lett.* **2012**, *80*, 95−98.
(42) Gianella, S.; Gaia, D.; Ortona, A. High Temperature Applications of SiSiC Cellular Ceramics. *Adv. Eng. Mater.* **2012**, *14*, 1074−1081.
(43) Nan, X.; Sullivan, C. An improved calculation of proximity-effect loss in high-frequency windings of round conductors. *PESC Record—IEEE Annual Power Electronics Specialists Conference*, 2003; Vol. *2*; pp 853−860.
(44) Saad, P. *Efficient and Wideband Power Amplifiers for Wireless Communications*; Chalmers University of Technology: Göteborg, 2012.
(45) Zhang, Z.; Chen, X. Regeneration reaction characteristics and mechanism model of K2CO3/Al2O3 sorbent for CO2 capture. *Asia-Pac. J. Chem. Eng.* **2021**, *16*, No. e2557.

https://doi.org/10.1021/acssuschemeng.5c10443
ACS Sustainable Chem. Eng. 2026, 14, 5922−5932